JOURNAL OF PROPULSION AND POWER
Vol. 26, No. 6, November–December 2010

Comparative Study of Spray Characteristics of Gas-Centered and Liquid-Centered Swirl Coaxial Injectors

Ji-Hyuk Im,* Seongho Cho,* and Youngbin Yoon†
Seoul National University, Seoul 151-742, Republic of Korea
and
Insang Moon
Korea Aerospace Research Institute, Daejeon 305-333, Republic of Korea

DOI: 10.2514/1.48436

This study investigated the spray and Sauter mean diameter characteristics of gas–liquid swirl coaxial injectors by measuring and analyzing spray angles and mean drop sizes. Two different types of gas–liquid swirl coaxial injectors were designed and tested for this experiment: 1) a gas-centered swirl coaxial injector and 2) a liquid-centered swirl coaxial injector. The spray patterns were obtained for both types of injectors. The spray angles of these liquid-centered swirl coaxial injectors showed a decreasing trend as a function of the momentum flux ratio over the conditions studied. Good agreement was generally achieved between the predicted and measured spray angles. On the other hand, with increasing momentum flux ratio, the spray angle of the gas-centered swirl coaxial injector initially decreased when the momentum flux ratios were relatively low, but the trend reversed over the high momentum flux ratio range studied. The Sauter mean diameter data of these two types of injectors were also obtained using an image-processing method. Results showed that the Sauter mean diameter distribution of the liquid-centered swirl coaxial injector had a solid cone shape, whereas the gas-centered swirl coaxial injector exhibited two distinct Sauter mean diameter distribution regimes. The gas-centered swirl coaxial injector had a solid cone shape along the centerline, and it had a hollow cone shape at the periphery.

Nomenclature

D_l	=	diameter of the liquid core, mm
d	=	diameter, mm
h	=	film thickness, μm
h_0	=	initial thickness of the liquid sheet, μm
i	=	number of tangential inlet
J	=	momentum flux ratio, $\rho_g u_g^2/\rho_l u_l^2$
K	=	injector constant, Rr_o/ir_p^2
L_R	=	recessed length of the inner orifice, mm
$\dot{m}$	=	mass flow rate, kg/s
R	=	swirl arm from axis of injector to center of tangential inlet, mm
Re	=	Reynolds number
RR	=	recess ratio, L_R/d_o
r	=	radius, mm
u	=	axial velocity, m/s
w	=	circumferential velocity, m/s
x_b	=	breakup length, mm
ΔP	=	pressure drop, MPa
θ	=	spray angle, deg
θ_0	=	equivalent spray angle without the gas stream, deg
μ	=	viscous coefficient, kg/m · s
ρ	=	density, kg/m^3

Subscripts

g	=	gas phase
l	=	liquid phase
o	=	orifice
p	=	tangential inlet

Received 7 December 2009; revision received 13 July 2010; accepted for publication 13 July 2010.

*School of Mechanical and Aerospace Engineering.
†Professor, School of Mechanical and Aerospace Engineering, 599 Gwanak-ro, Gwanak-gu; ybyoon@snu.ac.kr (Corresponding Author).

I. Introduction

SWIRL injectors are widely used in combustion devices of liquid rocket engines, gas turbine engines, and diesel engines. A swirl injector can generally achieve good atomization quality and high mixing efficiency. As shown in Fig. 1, the circumferential velocity component is first generated as the propellant enters through helical or tangential inlets producing a thin, swirling liquid sheet. A gas-filled hollow core is then formed along the centerline inside the injector due to centrifugal force of the liquid sheet. Because of the presence of the gas core, the discharge coefficient is generally low. In a swirl injector, the spray cone angle is controlled by the ratio of the circumferential velocity to the axial velocity and is generally wide compared with nonswirl injectors. The breakup process of the swirling liquid includes thinning and perforation of the liquid sheet, ligaments, and droplets. In the past, various experimental diagnostics and theoretical analyses were conducted over a broad range of operating conditions. Bayvel and Orzechowski [1] proposed that by assuming inviscid flow, the spray characteristics, such as the discharge coefficient, spray cone angle, and film thickness, are a function of injector design parameter, $K = Rr_o/ir_p^2$, where R is the swirl arm from the axis of the injector to the center of the tangential inlet, r_o and r_p are the radii of the orifice and tangential inlet, respectively, and i is the number of tangential inlets. Rizk and Lefebvre [2] studied the internal and external flow characteristics of a swirl injector and derived a correlation between the spray cone angle and film thickness, and they expressed the relationship as a function of injector geometry and liquid property. In their study, they assumed that only the pressure and viscous forces acted on the liquid flow inside the orifice.

Gas–liquid coaxial injectors are generally used in liquid bipropellant rocket engines when one propellant gets vaporized before reaching the thrust chamber. For liquid oxygen/liquid hydrogen (LOX/LH_2) engines, LH_2 is generally used as a coolant for regeneratively cooled thrust chambers, passing through the cooling channels and entering the chamber. For staged-combustion cycle engines, one

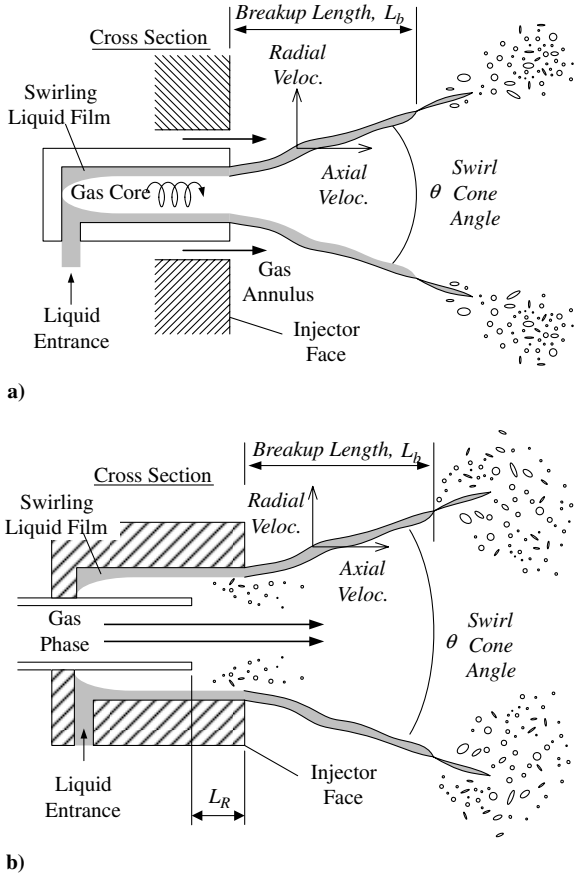

Fig. 1 Breakup mechanisms of a) the LCSC injector and b) the GCSC injector.

propellant is burned with a small amount of the other in the preburner, producing a hot gas mixture. Then this gas mixture passes through the turbine and is injected into the thrust chamber. The breakup of a swirl spray is largely due to hydraulic instability of the liquid sheet, and it can be significantly enhanced by the interaction between the liquid sheet and the gas injection of a gas–liquid coaxial injector. There are two common types of gas–liquid swirl coaxial injectors: 1) liquid-centered swirl coaxial (LCSC) injectors and 2) gas-centered swirl coaxial (GCSC) injectors. They are classified according to the type and location of swirling propellant.

In the few past decades, many studies were conducted to provide greater insight into the underlying mechanisms dictating the spray characteristics. Hardalupas and Whitelaw [3], for instance, investigated the spray patterns and Sauter mean diameter (SMD) for various geometric conditions, and they reported swirl injector design parameters in terms of droplet size and diffusion rate. Ingebo [4] identified an empirical correlation between the SMD and gas phase conditions according to gas species [e.g., $\mathrm{SMD}^{-1} = k(\rho_g u_g)^{1.33}$]. Miller et al. [5] investigated the combustion dynamics of a GCSC injector element using a single-element combustor rig. In their experiment, strong spontaneous instabilities were measured, and the frequencies of the strongest instabilities ranged from 1184 to 1721 Hz. The most amplified modes ranged from the first longitudinal mode for a 38.1 cm chamber to the third longitudinal mode for a 88.9 cm chamber. Soller et al. [6] investigated the combustion stability characteristics of a GCSC injector using LOX and kerosene. They also measured the chamber wall heat transfer as a function of propellant mixture ratio, chamber pressure, and coaxial injector recess length. Lightfoot and Danczyk [7] studied the nonuniformity of GCSC sprays and identified five basic types of nonuniformity: 1) centerline leaning, 2) bouncing, 3) oscillations, 4) axisymmetric pulsing, and 5) asymmetric pulsing.

In the present study, we investigated the spray characteristics of gas–liquid swirl coaxial injectors with a special emphasis given to two injector types: 1) liquid centered and 2) gas centered. The fundamental breakup mechanisms of the LCSC injector and the GCSC injector are schematically illustrated in Fig. 1. The spray breakup of these injectors is largely controlled by the interaction between the liquid and the gas, and it will be discussed in terms of the axial Reynolds number Re_l and the momentum flux ratio J in the current work. In particular, the spray patterns and spray angles will be presented for both of the injector types. Also, the mean drop sizes were measured and analyzed in this study. The SMD distributions will be presented.

II. Experimental Methods

A. Experimental Conditions

As shown in Fig. 2, two types of gas–liquid swirl coaxial injectors were designed and studied in the current work: 1) liquid-centered swirl with outer gas jet and 2) gas-centered jet with outer liquid swirl. A gas–liquid swirl coaxial injector with inner liquid swirl is hereafter referred to as the LCSC injector, and a gas–liquid swirl coaxial injector with an inner gas jet with outer liquid swirl is referred to as the GCSC injector. The orifice diameter d_o of the LCSC was 2.5 mm, and two tangential holes with a diameter d_p of 1 mm each were located at every 180 deg to generate the tangential velocity. The inner and outer diameters of the annular gap for the gas passage were 4 and 7 mm, respectively. Four inner liquid injectors were designed to

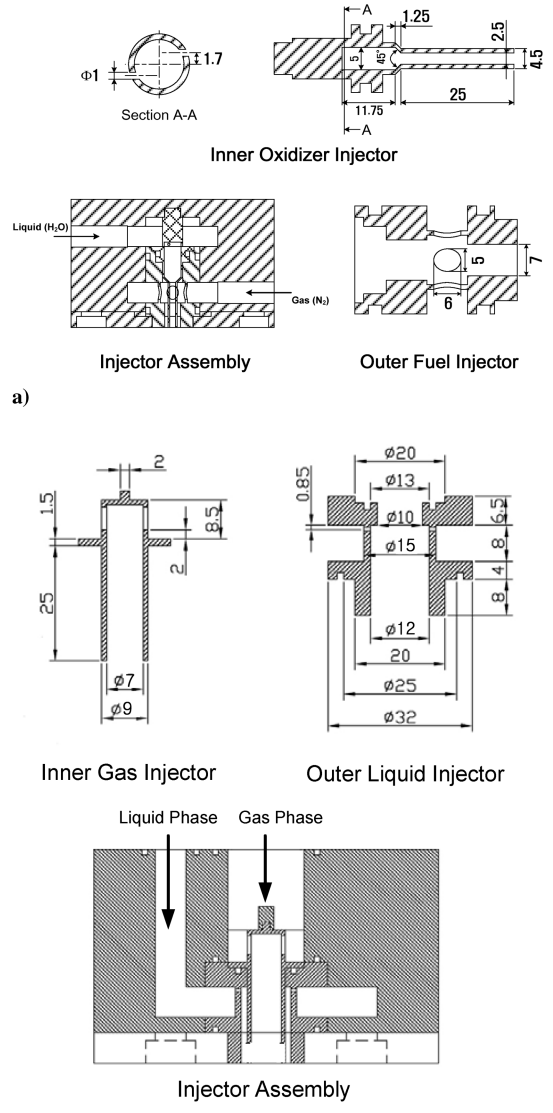

Fig. 2 Schematics of a) the LCSC injector and b) the GCSC injector (unit: mm).

Table 1 Experimental conditions and parameters

Simulant	Mass flow rate, g/s	Injection pressure, MPa	Axial Reynolds number	Momentum flux ratio
		LCSC Injector		
Water	17.27–31.98	0.20	2680	——
		0.27	3040	——
		0.34	3400	——
		0.42	3760	——
		0.50	4110	——
		0.7	4810	——
Air	0.77–7.40	——	——	0.02–3.01
		GCSC Injector		
Water	15.68–25.59	0.5	477	——
		0.6	517	——
		0.7	553	——
		0.8	587	——
		0.9	618	——
		1.0	648	——
		1.1	677	——
		1.2	704	——
Air	1.16–12.47	——	——	1–86

investigate the effects of recess length. The orifice of the inner liquid injector was recessed at 0, 1.25, 2.5, and 3.75 mm, which corresponds to 0, 0.5, 1.0, and 1.5 d_o, respectively. On the other hand, GCSC had an inner gas orifice with a diameter d_i of 7 mm. The gas was discharged in a jet form. The outer diameter of the inner gas injector was 9 mm. The diameter of the outer liquid orifice was 12 mm. Two tangential entries with a diameter of 0.7 mm were located at 180 deg. The recess lengths of the inner orifice were 4, 6, 8, 10, 12, 14, and 16 mm. The recess ratio RR is defined as the ratio of the recessed length L_R to the orifice diameter d_o, which can be expressed as Eq. (1):

$$RR = \frac{L_R}{d_o} \tag{1}$$

The detailed schematics of each injector can be found in Fig. 2.

The injection pressure differential of the liquid phase in the LCSC was varied from 0.2 to 0.7 MPa to correspond to a mass flow rate range of 17.27 to 31.98 g/s, respectively. The mass flow rate of the gas phase was controlled using a choked orifice and was varied from 0.77 to 7.40 g/s. The injection pressure differential of the liquid phase in the GCSC was varied from 0.4 to 1.2 MPa to correspond to a mass flow rate range of 15.68 to 25.59 g/s, respectively. Also, the mass flow rate of the gas phase was controlled using a choked orifice and was varied from 1.16 to 12.47 g/s. The experimental conditions are summarized in Table 1.

B. Experimental Techniques

The spray cone angle was measured using instantaneous spray images taken by indirect photography. A stroboscopic light source was used with a luminous time of less than 3 μs. A digital camera (Canon EOS 20D, 3504 × 2336) was used, and its exposure time was set so that only one flash of light could be taken per image without extra synchronization. Ten images were taken for each experimental case, and all images were averaged to accurately measure the spray cone angle. The deviations of data from the average spray angle were less than 6%.

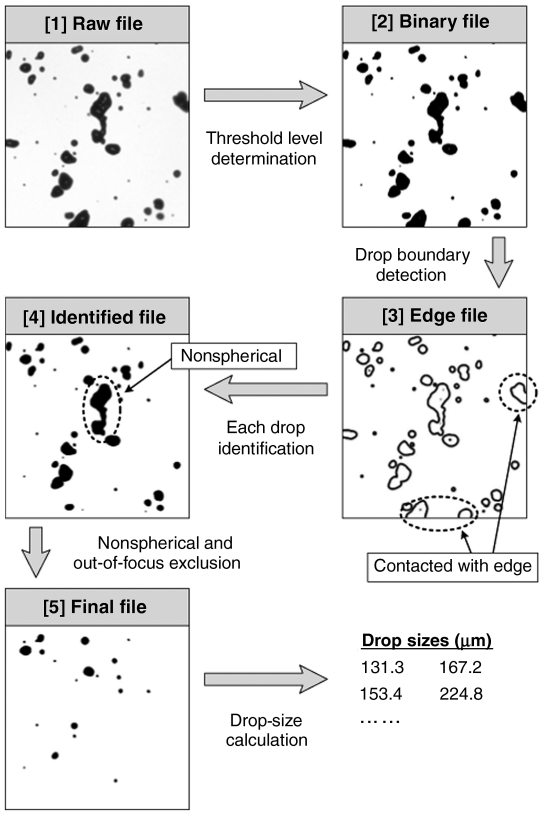

Fig. 3 Procedures of image-processing method for drop-size measurement.

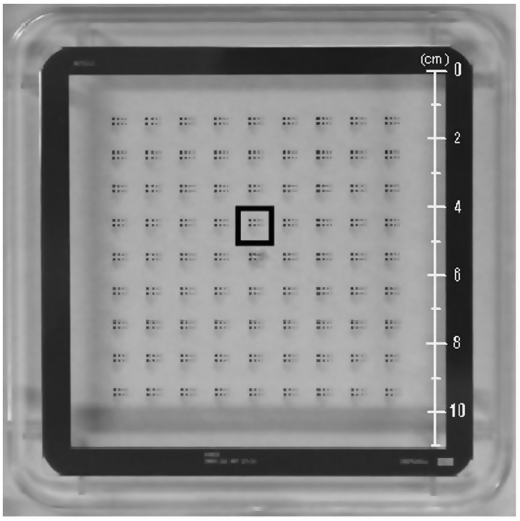

a)

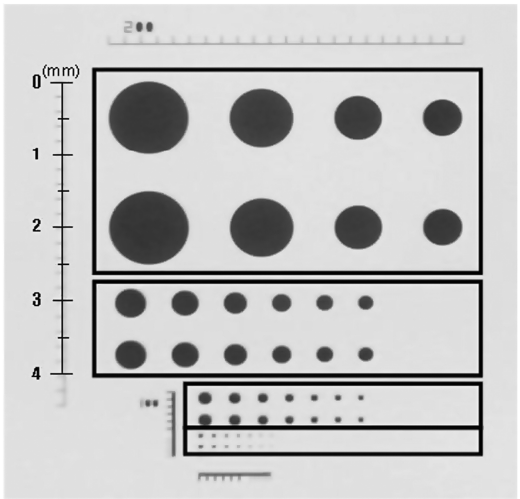

b)

Fig. 4 Glass reticle used for calibration of image-processing method: a) calibration reticle and b) four groups of circular shapes.

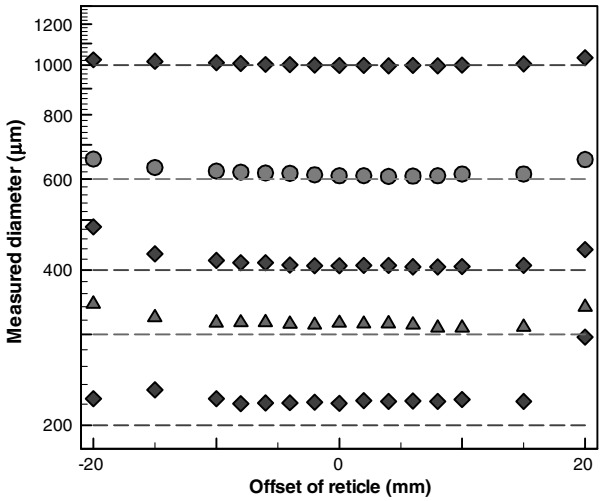

Fig. 5 Variation of measured size with shifting the calibration reticle back and forth from the focal plane.

The size of the droplets was obtained using an image-processing method. The droplet images were taken using a digital camera with high magnification lenses (Canon EF 180 mm $f/3.5$ L Micro USM and two Vivitar 2× teleconverters). A magnification ratio of 4.03 μm/pixel was obtained. In this study, the image-processing method followed the procedures shown in Fig. 3. In the first step, the raw files acquired by a digital camera with a high magnification ratio were converted into binary files in which the gray level intensities between the drops and the background could be distinguished from a proper threshold level. The threshold was determined to be 80% gray level from the intersection point between the maximum gradient line and the x axis on a gray level histogram of the image [8]. In the second step, droplet boundaries were detected by scanning for four adjacent pixels with the same intensity levels in the horizontal and vertical directions around the object pixel. In the next step, the boundaries consisting of a closed curve were identified as belonging to the same drop and were numbered in order from the top to the bottom of the image. During this pattern recognition step, the unconnected boundaries, such as those contacting the image edge, were excluded. In the final step, the area enclosed by identical droplet boundaries was calculated, and the droplet size was determined as the diameter of a spherical particle corresponding to the calculated area. Also, during this drop-sizing step, nonspherical particle images overlapped each other and out-of-focus droplets were eliminated.

The present method for drop sizing was validated using a calibration reticle. On the glass reticle, four groups of circular shapes were arranged by size, as shown in Fig. 4. The measured sizes of circular shapes on the reticle were compared with the known sizes of droplets, as shown in Fig. 5. The measured sizes were shown to be accurate and were within an error allowance of 10% for drops larger than 40 μm at a focal plane. The deviation from a known size decreased as the object size increased. Also, the variation of measured sizes was examined by shifting the calibration reticle back and forth from the focal plane to investigate the out-of-focus effect on the droplet size measurement. The measured size of large droplets was only slightly influenced by the offset from a focal plane, while the measured size of small droplets was significantly affected by the offset due to light diffraction. Increased offset made it impossible to distinguish the image of droplets from that of the background. However, the out-of-focus droplets were eliminated during the image-processing procedure. If the gradient at the edge of the droplets was smaller than a certain criterion, those droplets were determined to be the out-of-focus droplets and were eliminated during the drop-size calculations.

III. Results and Discussion

The breakup process of the swirl spray involves the hydraulic instability of the liquid sheet assisted by the aerodynamic instability of the ambient gas. Basically, the initial liquid film thickness h_0, the axial velocity u_0, and the circumferential velocity w_0 determine the spray angle and breakup length. Rizk and Lefebvre [2] used a theoretical approach to investigate the internal flow characteristics of pressure-swirl atomizers. They particularly examined the effects of atomizer dimensions and operating conditions on the spray cone angle, velocity coefficient, and the annular liquid film thickness at the discharge orifice. A general expression for the film thickness h was derived as a function of atomizer dimensions, liquid properties, and liquid injection pressure:

$$h^2 = \frac{1560\dot{m}_l\mu_l}{\rho_l d_o \Delta P_l}\frac{1+X}{(1-X)^2} \tag{2}$$

where $X = (d_o - 2h)^2/d_o^2$.

The breakup mechanism of a gas–liquid swirl coaxial spray is largely controlled by the transfer of kinetic energy to the liquid by the gas. Therefore, the momentum flux ratio between the liquid and gas phases is one of the key parameters in gas–liquid coaxial sprays. Lasheras and Hopfinger [9] theoretically and experimentally investigated the breakup characteristics of jets by varying the momentum flux ratio and Weber number, and they derived the following correlation between the jet core breakup length and the momentum flux ratio:

$$\frac{x_b}{D_l} = \frac{6}{J^{0.5}} \tag{3}$$

where $J = \rho_g u_g^2/\rho_l u_l^2$.

Recess is a geometric configuration in which the exit of the inner orifice is located inward relative to the outer orifice. The recess region can enhance mixing efficiency and affect flame stability through the internal mixing of the propellants [10]. In previous studies, the momentum flux ratio and the liquid Reynolds number were used as operating parameters, and the recess length was selected as a geometric parameter.

A. Spray Patterns

The spray patterns of the LCSC and GCSC are shown in Fig. 6. The spray patterns of the LCSC became more similar to those of nonswirling, shear coaxial jets as the momentum flux ratio increased. The swirling liquid sheet contracted into the centerline in response to the high-velocity annular gas stream and its spray patterns became narrow solid cone shaped. The liquid could not preserve the form of the liquid sheet and disintegrated into droplets immediately after being discharged from the orifice. As the liquid flowed downstream, the droplets coalesced, and then secondary breakup occurred. Subsequently, the LCSC sprays appeared macroscopically similar to the shear coaxial sprays as the momentum flux ratio increased. The spray distributions of the LCSC are shown in Fig. 7. A large amount of the liquid mass concentrated around the center, which was the typical mass distribution of shear coaxial sprays. Under high momentum flux ratio conditions, self-pulsation occurred. Self-pulsation is the unstable phenomenon that occurs due to severe interactions between the liquid and gas, and it is accompanied by strong spray oscillations and intensive noise. Self-pulsation was first discovered in the mid-1970s in gas–liquid coaxial injectors in Russia, and some experimental studies have been performed since then. Detailed results of the self-pulsation are summarized in [11–13].

The GCSC sprays maintain the swirl shape even at a high momentum flux ratio condition. Along the centerline, the small droplets atomized inside the injector are largely due to interactions between the liquid and gas in the space confined by the outer injector wall. Any liquid that was not atomized inside the injector was discharged in the form of a sheet at the perimeter. The liquid was not completely atomized inside the injector under the current geometric configurations and operating conditions. In other experimental conditions, liquid can also be, however, fully atomized inside the injector. Lightfoot and Danczyk [7], for instance, performed experimental studies on a GCSC injector and reported that the liquid was atomized

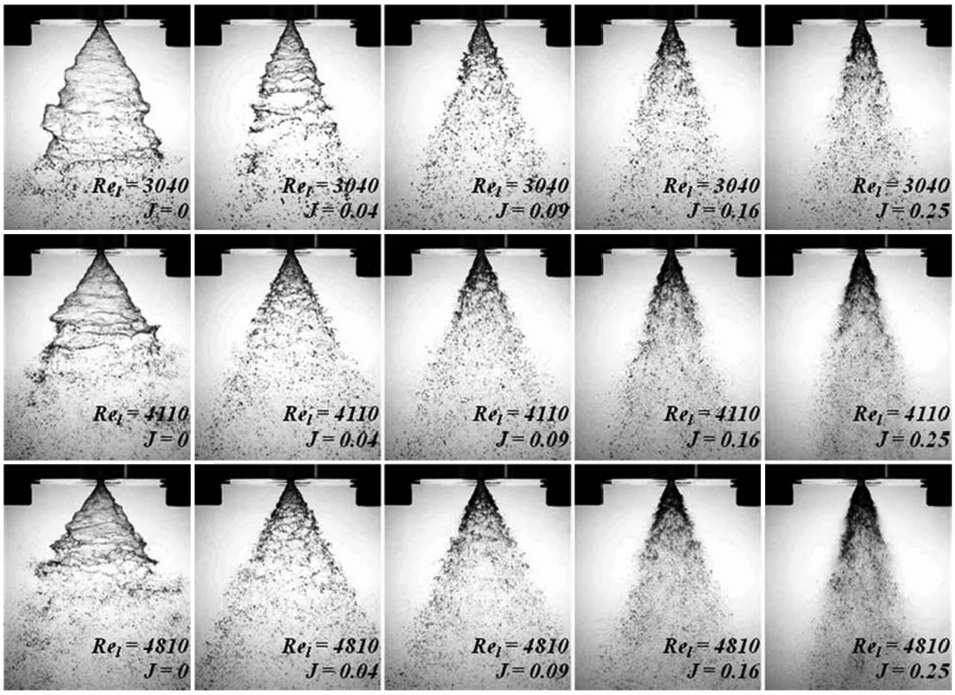

a)

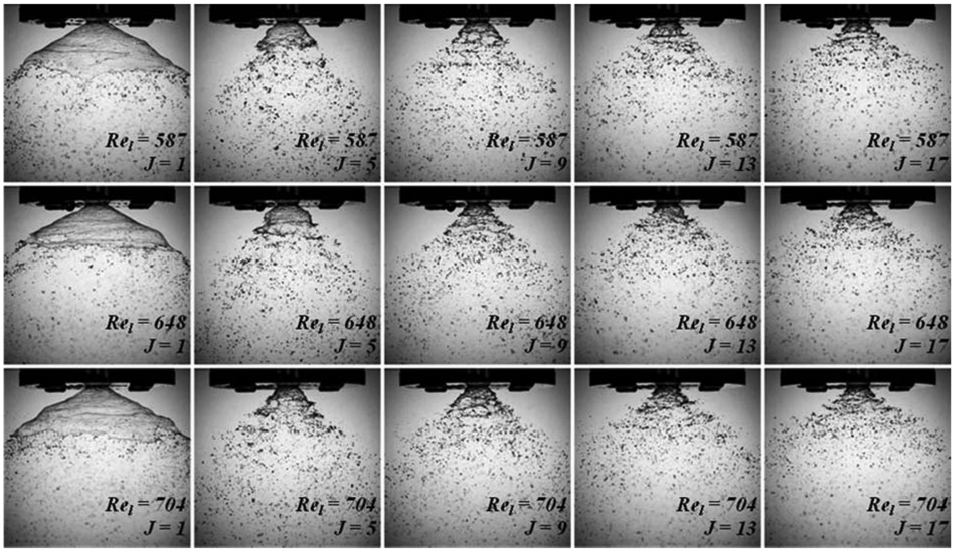

b)

Fig. 6 Spray patterns of a) the LCSC injector and b) the GCSC injector.

into droplets inside the injectors under certain operating conditions. However, if the breakup of the liquid sheet was completed inside the injector, the heat transfer to the injector wall by means of combustion would be severe in the actual combusting environment. The spray angle of the liquid sheet increased as the momentum flux ratio increased for the gas-centered swirl injector. This trend was the opposite of the result from using the LCSC injector and will be further discussed in Sec. III.B.

B. Spray Angle

The spray angle characterizes the spatial distribution of droplets; thus, it has a strong influence on the ignition and steady-state performance as well as the chamber wall cooling. In this study, the spray angle is defined as the angle between both sides of the spray edges obtained by processing the average spray images.

Here, the liquid and gas interactions were characterized as a function of momentum flux ratio, and the Reynolds number Re_l based on a film thickness can be expressed as

$$Re_l = \frac{\rho_l u_l h_0}{\mu_l} \tag{4}$$

Figure 8 shows the spray angle of the LCSC as a function of momentum flux ratio for various values of Re_l. The spray angle decreased as the momentum flux ratio increased. The liquid sheet contracted into the center by momentum transfer from the high-velocity annular gas stream to the liquid sheet. Above a certain momentum flux ratio, the decreasing rate of the spray angle was reduced. At a fixed gas phase momentum, the spray angle increased with increasing Re_l because the liquid sheet's large momentum at high Re_l value, which leads to the recovery of the spray angle of the liquid sheet itself. Considering that the deformation of the liquid sheet is due to the momentum transfer between two different phases, the spray angle of the LCSC could be calculated using a momentum conservation equation. The momentum conservation for each phase can be written as follows:

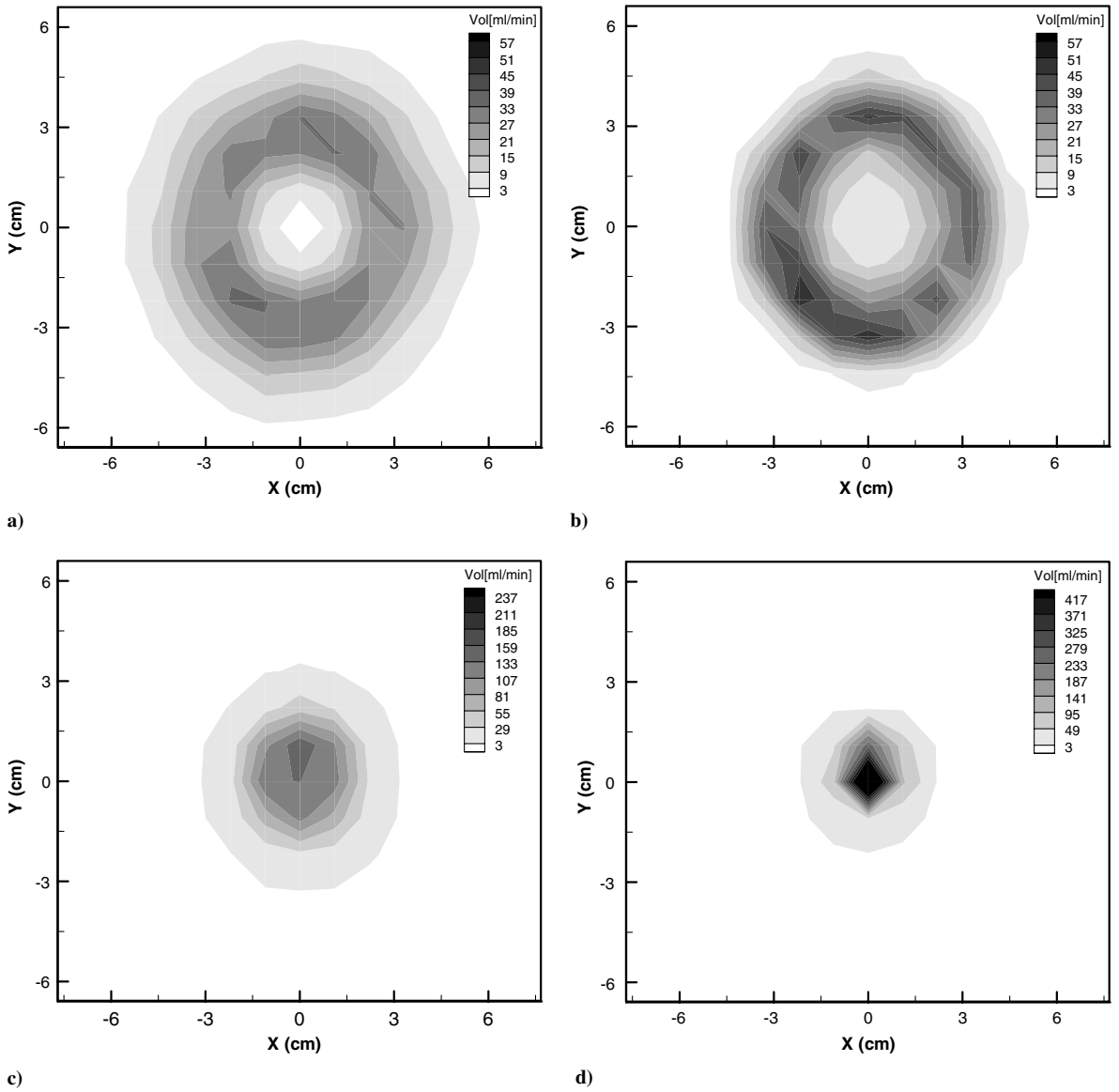

Fig. 7 Spray distributions measured by mechanical patternator with increasing momentum flux ratio at $Re_l = 4110$: a) $J = 0$, b) $J = 0.05$, c) $J = 1.47$, and d) $J = 2.43$.

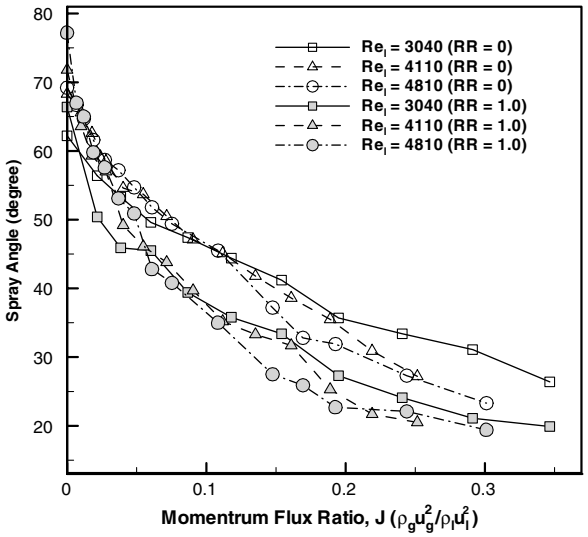

Fig. 8 Spray angle of the LCSC injector as a function of momentum flux ratio J for various Re_l and recess ratios.

$$\dot{m}_l u_l + \dot{m}_g u_g = (\dot{m}_l + \dot{m}_g)u \qquad \dot{m}_l w_l + \dot{m}_g w_g = (\dot{m}_l + \dot{m}_g)w \tag{5}$$

where u is the axial velocity of the liquid and gas mixture, and w is the circumferential velocity of the liquid and gas mixture. The gas phase does not have a circumferential velocity component, but it does have the radial velocity component due to diffusion to the radial direction. Therefore, w_g indicates the radial velocity of the gas phase. The spray angle is inferred to be the ratio of the circumferential velocity to the axial velocity of the liquid–gas mixture as follows:

$$\tan\frac{\theta}{2} = \frac{w}{u} = \frac{\dot{m}_l w_l + \dot{m}_g w_g}{\dot{m}_l u_l + \dot{m}_g u_g} = \frac{\dot{m}_l u_l \tan(\theta_l/2) + \dot{m}_g u_g \tan(\theta_g/2)}{\dot{m}_l u_l + \dot{m}_g u_g} \tag{6}$$

where θ_l and θ_g are the spray angles of the liquid and gas phases, respectively. Using Eq. (6), the spray angles of the LCSC were calculated and plotted in Fig. 9. In general, the calculated spray angles matched well with the measured data for injectors without the recess. However, the measured spray angles were noticeably smaller than the predicted spray angles. It is likely due to the impingement and friction losses along the internal injector wall.

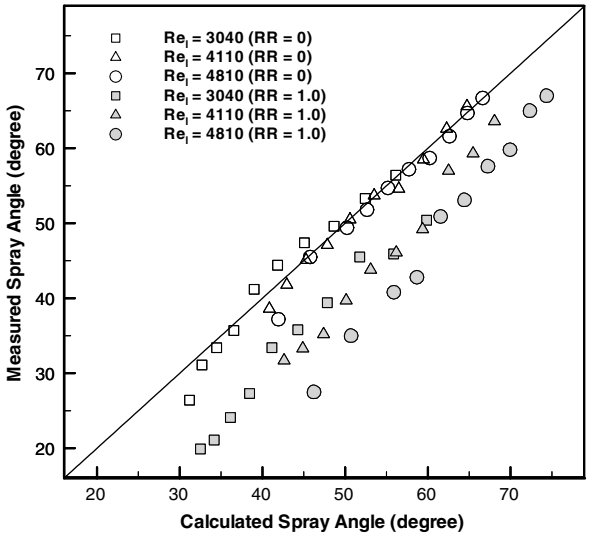

Fig. 9 A comparison of the measured and calculated spray angles of the LCSC injector for various recess lengths.

The spray angle of the GCSC is shown in Fig. 10. Similar to the LCSC, the spray angle of the GCSC also decreased as the momentum flux ratio increased over the low momentum flux ratio range studied in this work. The interspace gas between the liquid and gas propellants was entrained into the high-velocity central gas stream and liquid sheet, as shown in Fig. 11. The interspace ambient gas was surrounded by the liquid sheet, and the volume of the interspace ambient gas was limited; thus, the pressure of the interspace ambient gas P_{is} decreased as the interspace ambient gas was entrained. The entrainment of the outer ambient gas for which the volume is very large, however, could be neglected. In this case, the pressure of the outer ambient gas would be greater than that of the interspace ambient gas. As the momentum flux ratio increased, the spray angle of the GCSC decreased due to the increase in the amount of entrained interspace ambient gas. Therefore, the liquid sheet bent toward the center of the spray due to the force balance. However, above some momentum flux ratios, the spray angle of the GCSC started to increase with increasing momentum flux ratio. This suggests that there may be at least two physical processes involved in interaction between the inner gas jet and the outer swirling liquid, and they are sensitive to the momentum flux ratio. As the momentum flux ratio increased, the mass flow rate of the gas phase was increased, causing higher inner gas pressures. Therefore, the outward pressure acting on

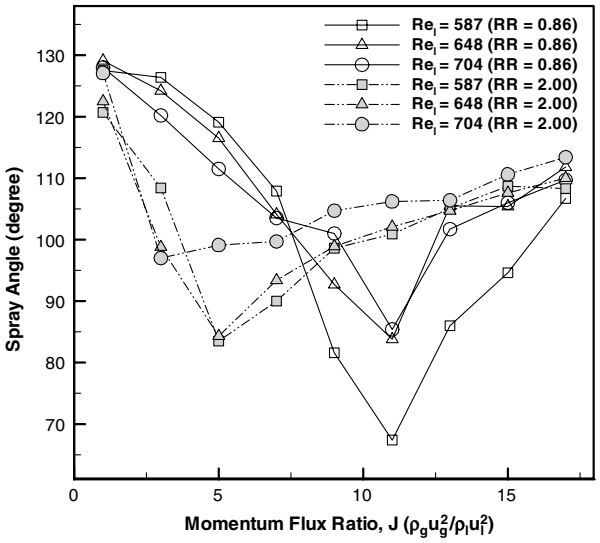

Fig. 10 Spray angle of the GCSC injector as a function of momentum flux ratio J for various Re_l and recess ratios.

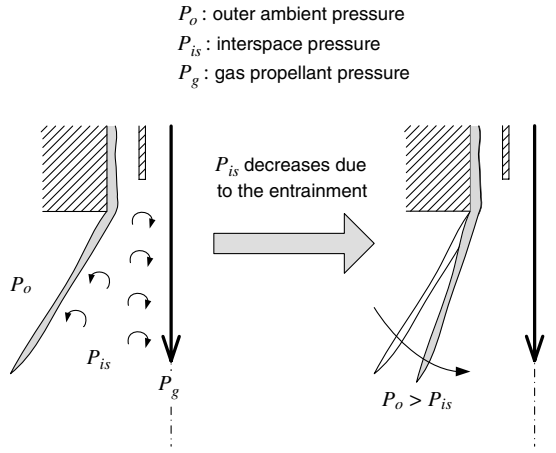

Fig. 11 Schematics of spray angle reduction at low momentum flux ratio in the GCSC injector.

the liquid sheet could be higher and, as the liquid flows injected from the nozzle exit, the liquid sheet spread out due to the outward force. Also, the higher gas-core pressure restricted outer swirling liquid flow. The GCSC injectors used in this study were a recess configuration. The gas and liquid interacted and mixed inside the injector, and the gas core was filled with the center gas stream. Thus, the flow restriction made liquid film thickness thinner, as shown in Fig. 12, and accelerated the liquid swirling velocity. As a result, it may have increased the circumferential velocity of the outer liquid flow sufficiently enough to increase the spray angle at high momentum flux ratios. However, more needs to be learned about the complex processes involved in this liquid–gas interaction to gain better insight into the underlying mechanisms.

Based on the measured data, the empirical correlations for the normalized spray angles of the LCSC and GCSC were derived and could be written as

$$\theta/\theta_0 = 0.35Re^{0.125}e^{-4.067J} - 0.06RR \tag{7}$$

$$\theta/\theta_0 = 0.61Re^{0.08}e^{-0.0657J} \tag{8}$$

for low J, and

$$\theta/\theta_0 = 0.33Re^{0.08}e^{0.02518J}RR^{0.33}$$

for high J, where θ_0 is the equivalent spray angle without the gas stream. The normalized spray angle depended exponentially on the momentum flux ratio. The empirical relations of the spray angle are plotted in Fig. 13. The normalized spray angle of the LCSC could be described by Eq. (7). The spray angle decreased rapidly with increasing momentum flux ratio due to the momentum transfer from the annular gas stream to the liquid phase. The effects of the recess ratio were unclear due to insufficient data in this work. For the GCSC,

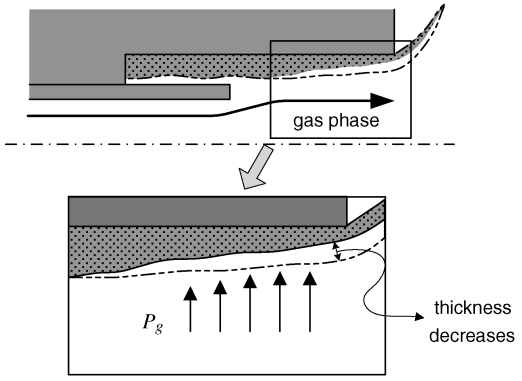

Fig. 12 Schematics of film thickness reduction inside the GCSC injector.

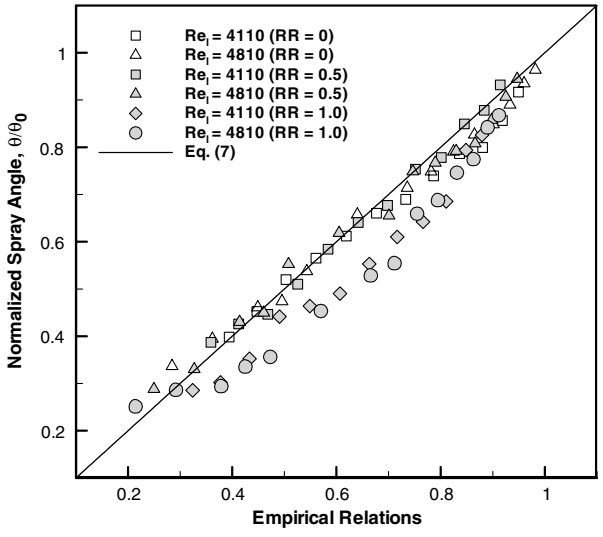

a)

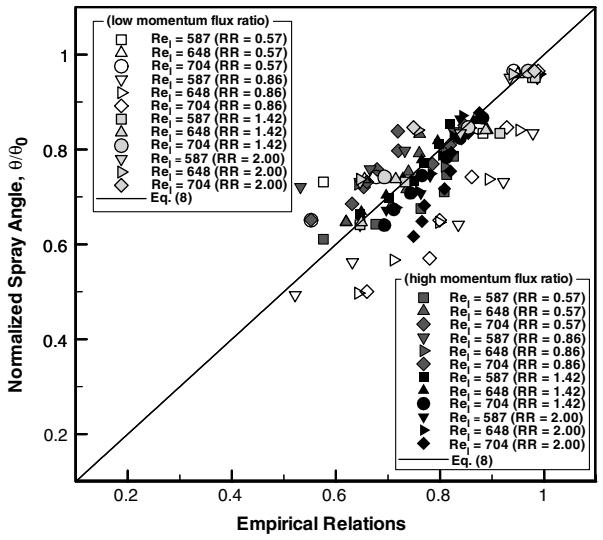

b)

Fig. 13 Empirical relations of the spray angle of a) the LCSC injector and b) the GCSC injector.

as can be seen in Eq. (8), the spray angle decreased with increasing momentum flux ratio in the low momentum flux ratio. However, at higher momentum flux ratios, the spray angle increased as the momentum flux ratio increased, and the recess ratio also exhibited significant effects on the spray angle. The R square can be used to better understand the scatter of data from by curve fitting. The R square in Fig. 13a was 0.95, showing a good curve fitting with experimental data. The R square in Fig. 13b was 0.64. It suggests that the empirical correlation may not represent the data for the GCSC injectors. However, over the high momentum flux ratio range, the curve fitting appeared to be much better for the GCSC.

C. Mean Drop Size

The mean drop size is important, because it can be used to represent the quality of atomization, and high atomization quality leads to rapid vaporization and better mixing. Many past studies have concentrated on predicting the mean drop size and distribution [14]. In this work, the mean drop sizes were measured using the previously described image-processing method for the LCSC and GCSC. The number of counted droplets exceeded 3000. Since the concentration of droplets near the exit of the orifice was too dense, direct images of the droplets could not be taken; thus, the measurements of the LCSC were taken 10 cm downstream from the exit of the orifice where measurement was possible. On the contrary, the measurement location of the GCSC was 3 cm downstream from the exit of the orifice due to the large spray angle.

Figure 14 shows the radial profile of the SMD distributions of the LCSC. The measured SMD distribution exhibits a typical distribution of the solid cone or the shear coaxial spray. The droplets along the centerline were very large, while the droplets at the perimeter were relatively small. In some cases, self-pulsations were also observed. Details on the effects of the self-pulsations are available in [11–13].

The SMD distribution of the GCSC is shown in Fig. 15. The radial profile in the GCSC is different from that in the LCSC. Along the centerline, the SMD decreased as the radial distance increased; however, above certain radial locations, the SMD increased with increasing radial distance increases. It was clear that the effect of the inner gas jet became much less significant in terms of SMD at the injector perimeter. Along the centerline, small droplets inside the injector were entrained into an inner high-velocity gas stream, and the coalescence of these small droplets occurred. As a result, there were also large droplets along the centerline where the gas shear interaction would be at maximum. At the perimeter, the droplets were formed by breaking up the outer liquid sheet.

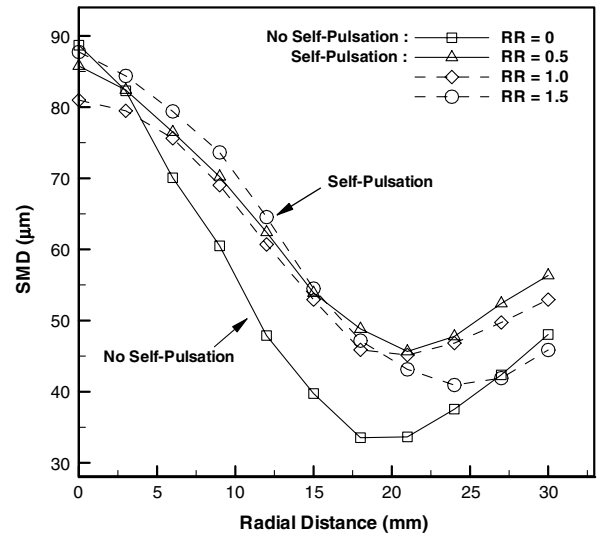

Fig. 14 The radial profile of the SMD distribution in the LCSC spray at $Re_l = 2680$ and $J = 2.43$ for various recess ratios at $z = 10$ cm.

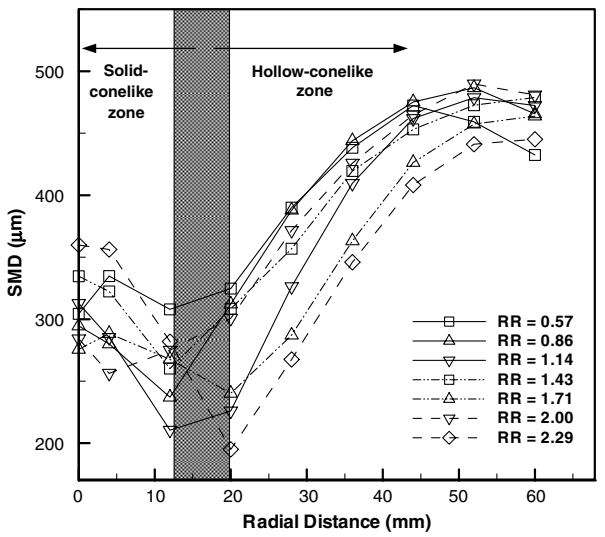

Fig. 15 The radial profile of the SMD distribution in the GCSC injector at $Re_l = 587$ and $J = 50$ for various recess ratios ($z = 3$ cm).

IV. Conclusions

Two types of gas–liquid swirl coaxial injectors were designed and analyzed in the current work. The spray characteristics of each gas–liquid swirl coaxial injector type were studied by measuring the spray angle and mean drop diameter. The spray pattern of the LCSC showed a solid cone shape over the entire momentum flux ratio range studied. As for the spray pattern of the GCSC, it exhibited two distinct zones: 1) a gas-dominant zone containing fine droplets along the centerline and 2) a liquid-dominant zone maintaining a liquid sheet in the form of a hollow cone at the perimeter. Images were captured, and the spray angles were measured. The images of the LCSC and GCSC sprays differed with varying momentum flux ratio. The spray angle of the LCSC decreased as the momentum flux ratio increased. Also, this behavior could be well predicted using the momentum conservation. For the GCSC, the spray angle decreased with increasing momentum flux ratio over the low momentum flux ratio range, but the trend reversed at high momentum flux ratios. The regime in which the spray angle decreased with the momentum flux ratio could be explained by the force balance between the outer ambient gas pressure and the interspace ambient gas pressure. The increase in spray angle with increasing momentum flux ratio was postulated to be due to increases in inner gas stream pressure and circumferential velocity of the outer liquid sheet. However, more work is needed to gain better insight into the detailed underlying mechanisms.

The SMD was also measured using an image-processing method in this work. The SMD distribution of the LCSC showed a solid conelike shape. The SMD along the centerline was the largest with smaller sizes at the perimeter. For the GCSC, it showed two distinct SMD distributions. Along the centerline, the SMD distribution of the GCSC was a solid conelike shape, whereas it showed a hollow conelike shape at the perimeter.

Acknowledgments

We are grateful for the financial support from the National Space Laboratory Program (S10801000194-08A0100-19410), Grants for Interdisciplinary Research (2009-0053283) through the National Research Foundation of Korea funded by the Ministry of Education, Science, and Technology, the Top Brand Project of the Korea Aerospace Research Institute, and the Institute of Advanced Aerospace Technology.

References

[1] Bayvel, L., and Orzechowski, Z., *Liquid Atomization*, Taylor and Francis, Philadelphia, 1993.

[2] Rizk, N. K., and Lefebvre, A. H., "Internal Flow Characteristics of Simplex Swirl Atomizer," *Journal of Propulsion and Power*, Vol. 1, No. 3, 1985, pp. 193–199. doi:10.2514/3.22780

[3] Hardalupas, Y., and Whitelaw, J., "Characteristics of Sparys Produced by Coaxial Airblast Atomizers," *Journal of Propulsion and Power*, Vol. 10, No. 4, 1994, pp. 453–460. doi:10.2514/3.23795

[4] Ingebo, R., "Gas Property Effects on Dropsize of Simulated Fuel Sprays," *Journal of Propulsion and Power*, Vol. 7, No. 4, 1991, pp. 467–472. doi:10.2514/3.23350

[5] Miller, K., Sisco, J., Nugent, N., and Anderson, W., "Combustion Instability with a Single-Element Swirl Injector," *Journal of Propulsion and Power*, Vol. 23, No. 5, 2007, pp. 1102–1112. doi:10.2514/1.26826

[6] Soller, S., Wagner, R., Kau, H. P., Martin, P., and Mäding, C., "Combustion Stability Characteristics of Coax-Swirl Injectors for Oxygen/Kerosene," AIAA Paper 2007-5563, 2007.

[7] Lightfoot, M. D. A., and Danczyk, S. A., "Spray Nonuniformities in Gas-Centered Swirl-Coaxial Injectors," *11th Triennial International Conference on Liquid Atomization and Spray Systems*, 2009.

[8] Kim, I., and Lee, S., "A Simple Technique for Sizing and Counting Spray Drops Using Digital Image Processing," *Experimental Thermal and Fluid Science*, Vol. 3, No. 2, 1990, pp. 214–221. doi:10.1016/0894-1777(90)90089-P

[9] Lasheras, J., and Hopfinger, E. J., "Liquid Jet Instability and Atomization in a Coaxial Gas Stream," *Annual Review of Fluid Mechanics*, Vol. 32, No. 1, 2000, pp. 275–308. doi:10.1146/annurev.fluid.32.1.275

[10] Mayer, W., Schik, A., Vielle, B., Chauveau, C., Gokalp, I., Talley, D., and Woodward, R., "Atomization and Breakup of Cryogenic Propellants Under High-Pressure Subcritical and Supercritical Conditions," *Journal of Propulsion and Power*, Vol. 14, No. 5, 1998, pp. 835–842. doi:10.2514/2.5348

[11] Im, J. H., Kim, D., Han, P., Yoon, Y., and Bazarov, V. G., "Self-Pulsation Characteristics of a Gas–Liquid Swirl Coaxial Injector," *Atomization and Sprays*, Vol. 19, No. 1, 2009, pp. 57–74. doi:10.1615/AtomizSpr.v19.i1.40

[12] Bazarov, V. G., "Self-Pulsation in Coaxial Injectors with Central Swirl Liquid Stage," AIAA Paper 1995-2358, 1995.

[13] Bazarov, V. G., and Yang, V., "Liquid-Propellant Rocket Engine Injector Dynamics," *Journal of Propulsion and Power*, Vol. 14, No. 5, 1998, pp. 797–806. doi:10.2514/2.5343

[14] Lefevbre, A. H., *Atomization and Sprays*, Hemisphere, New York, 1989.

E. Kim
Associate Editor